



Effect of Al content on the corrosion behavior and mechanism of $\text{Al}_x\text{CoCrFeNi}$ high-entropy alloys

Yi Wang ^{a,b}, Guanglong Li ^{a,b,*}, Hao Qi ^{a,b}, Wei Zhang ^{a,b}, Ruirun Chen ^c, Ruiming Su ^{a,b}, Yingdong Qu ^{a,b,**}

^a School of Materials Science and Engineering, Shenyang University of Technology, Shenyang, 110870, China

^b Key Laboratory of Light Metal Materials and Engineering at Universities of Liaoning Province, Shenyang, 110870, China

^c National Key Laboratory for Precision Hot Processing of Metals, Harbin Institute of Technology, 150001, China



ARTICLE INFO

Keywords:

High-entropy alloy
 AlCoCrFeNi
 Passivation film
 Crystal structure
 Corrosion resistance
 Corrosion mechanism

ABSTRACT

Al addition is known to improve the tensile strength and high-temperature oxidation behavior of the $\text{Al}_x\text{CoCrFeNi}$ high-entropy alloy (HEA). However, the corrosion behavior and mechanisms associated with these HEAs remain unclear. The corrosion resistance of structural materials is as important as their mechanical properties. In this study, $\text{Al}_x\text{CoCrFeNi}$ HEAs with different molar ratios of Al ($x = 0.0, 0.5, 1.0$, and 1.5) and various crystal structures (FCC, FCC + BCC, and BCC phases) were prepared, and their corrosion behavior and mechanisms were studied, which revealed a competitive relationship between the Al and Cr passivation films. The thickness of the Al passivation film increased with increasing Al content, which was found to be the main reason for the decrease in the corrosion resistance of the $\text{Al}_x\text{CoCrFeNi}$ HEAs. The corrosion type of the $\text{Al}_x\text{CoCrFeNi}$ HEA changed from pitting corrosion to selective corrosion with increasing Al content, and the corroded elements changed from (Co, Cr, Fe, and Ni) to (Al and Ni) and then (Al, Ni, and Co). Accordingly, the corrosion mechanisms associated with the $\text{Al}_x\text{CoCrFeNi}$ HEAs were elucidated.

1. Introduction

High-entropy alloys (HEAs) are novel metallic materials comprising metal elements with equal or nearly equal atomic ratios. Compared to traditional metal materials, HEAs have unique face-centered cubic (FCC) or body-centered cubic (BCC) crystal structures or are mixed-structure solid solutions [1]. $\text{Al}_x\text{CoCrFeNi}$, first reported in 2008 [2], is an extensively investigated HEA owing to its adjustable and excellent mechanical properties [3]. The atomic radius of Al is 14% larger than those of the other constituent elements in $\text{Al}_x\text{CoCrFeNi}$; hence, Al is considered to be a stabilizer of the BCC phase in an $\text{Al}_x\text{CoCrFeNi}$ HEA [4,5]. The quality of the alloy decreased, whereas the tensile strength and high-temperature oxidation behavior of the $\text{Al}_x\text{CoCrFeNi}$ HEA improved with increasing Al content [6–9]. However, the corrosion-resistance behavior of $\text{Al}_x\text{CoCrFeNi}$ HEAs with high Al contents remains unclear.

Shi et al. [10] found that the corrosion resistance of $\text{Al}_x\text{CoCrFeNi}$ ($x = 0.3, 0.5, 0.7$) HEAs in 3.5 wt% NaCl solution decreased with increasing Al content. However, Qiu et al. [11] found that $\text{Al}_{0.6}\text{CoCrFeNi}$

and $\text{Al}_{0.9}\text{CoCrFe}$ alloys exhibited lower corrosion current densities (i_{corr}) than CoCrFeNi and $\text{Al}_{0.3}\text{CoCrFeNi}$ in 0.6 M NaCl solution. Kao et al. [12] found that the passivation behavior of $\text{Al}_x\text{CoCrFeNi}$ ($x = 0, 0.25, 0.5$, and 1.0) HEAs in H_2SO_4 solution degraded with increasing Al content during dispersion of the passivation film. However, the corrosion resistance increased with increasing Al content in supercritical water [13]. These contradictory findings indicate that the influence of the Al content on the corrosion resistance of an $\text{Al}_x\text{CoCrFeNi}$ HEA is unclear. Örnek et al. [14] studied low-chromium, high-strength hybrid steels and found that the presence of Al enhanced the role of Cr in forming a spontaneously passive and protective surface, resulting in exceptional corrosion resistance in chloride-containing solutions. Hence, the corrosion resistance of $\text{Al}_x\text{CoCrFeNi}$ HEAs must be investigated further.

Moreover, the corrosion mechanisms associated with $\text{Al}_x\text{CoCrFeNi}$ HEAs with various phases remain unclear. Izadi et al. [15] reported that the amount of the BCC phase increased with increasing Al content, which deteriorated the corrosion behavior of the $\text{Al}_x\text{CoCrFeNi}$ ($x = 0.7, 0.85$, and 1.0) HEAs. Therein, only the effect of the BCC phase was

* Corresponding author. School of Materials Science and Engineering, Shenyang University of Technology, Shenyang, 110870, China.

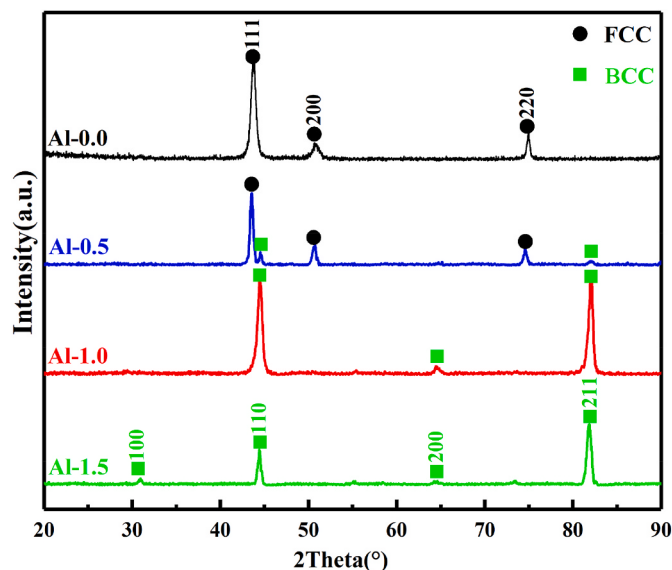
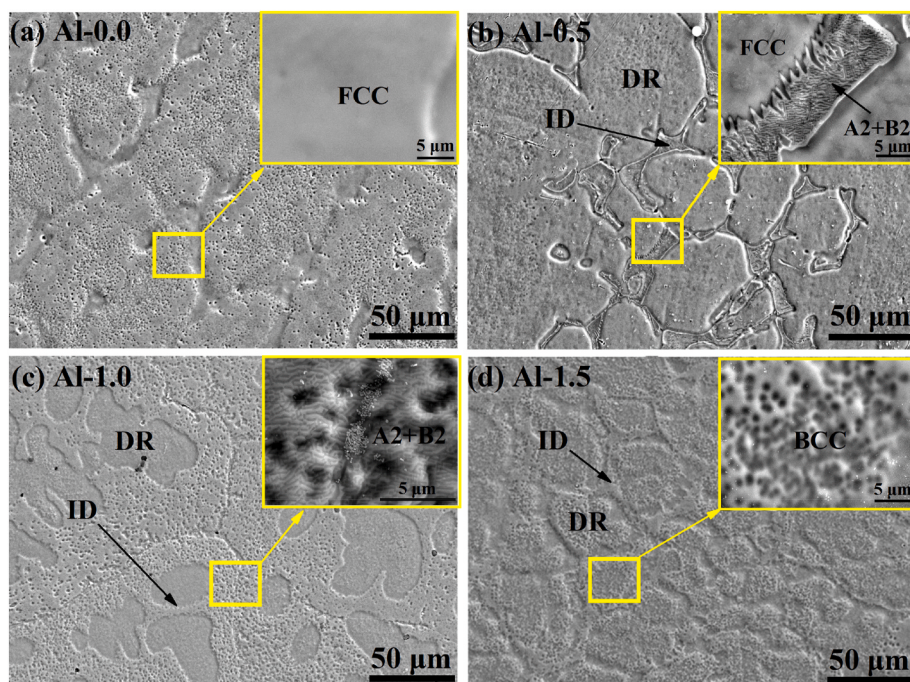
** Corresponding author. School of Materials Science and Engineering, Shenyang University of Technology, Shenyang, 110870, China.

E-mail addresses: liuguanglong1990@163.com (G. Li), quydong@sut.edu.cn (Y. Qu).

Table 1

Nominal and actual chemical compositions of HEA specimens.

ID	HEA systems		Element (at.%)				
			Al	Co	Cr	Fe	Ni
Al-0.0	$\text{Al}_{0.0}\text{CoCrFeNi}$	Nominal	0	25.00	25.00	25.00	25.00
		Actual	0	24.86	25.05	25.21	24.88
Al-0.5	$\text{Al}_{0.5}\text{CoCrFeNi}$	Nominal	11.11	22.22	22.22	22.22	22.22
		Actual	11.03	22.17	22.50	22.18	22.12
Al-1.0	$\text{Al}_{1.0}\text{CoCrFeNi}$	Nominal	20.00	20.00	20.00	20.00	20.00
		Actual	19.83	20.06	20.35	19.94	19.82
Al-1.5	$\text{Al}_{1.5}\text{CoCrFeNi}$	Nominal	27.27	18.18	18.18	18.18	18.18
		Actual	27.50	17.70	18.38	18.19	18.23

**Fig. 1.** XRD spectra of as-cast $\text{Al}_x\text{CoCrFeNi}$ HEAs.**Fig. 2.** SEM micrographs of as-cast $\text{Al}_x\text{CoCrFeNi}$ HEAs.

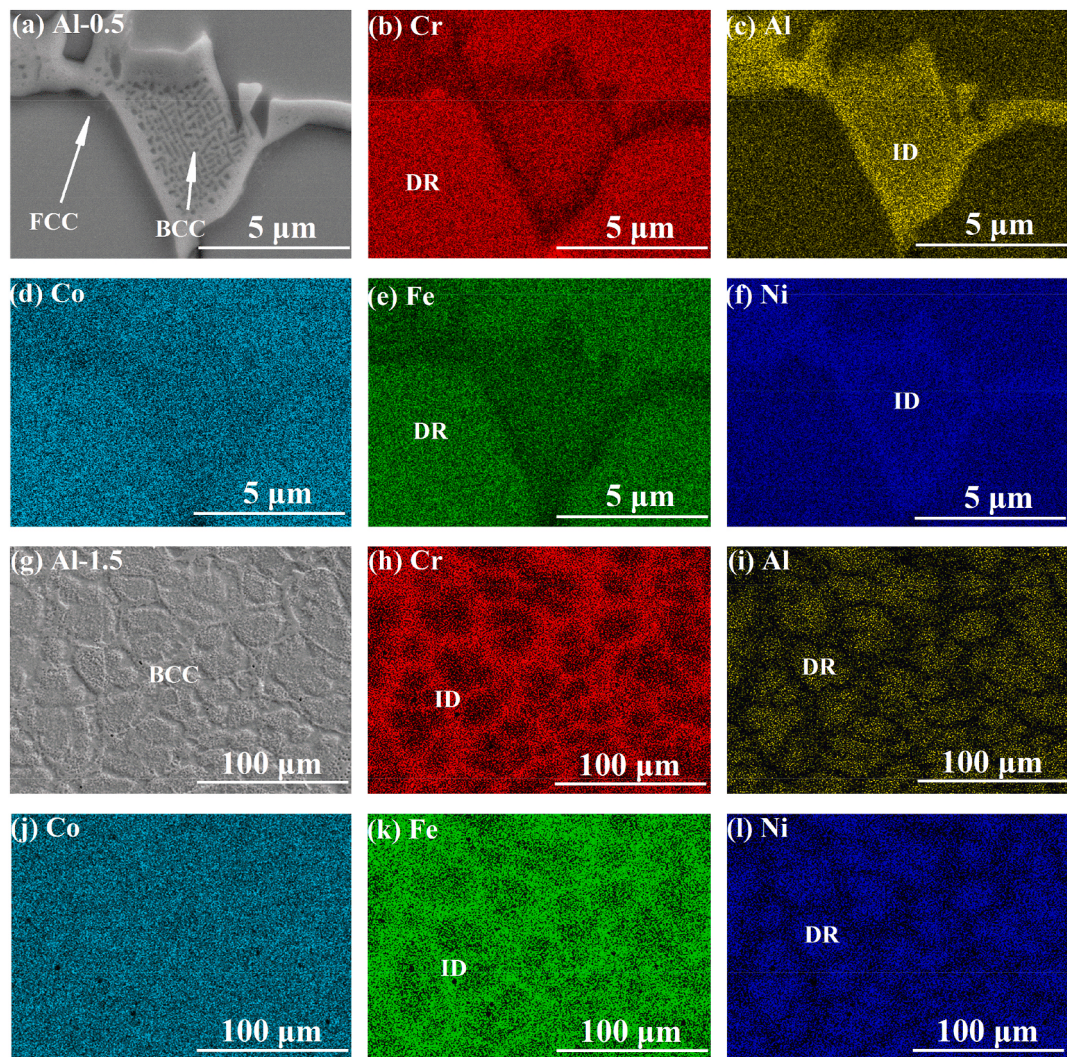


Fig. 3. EDS results for the Al-0.5 and Al-1.5 HEAs.

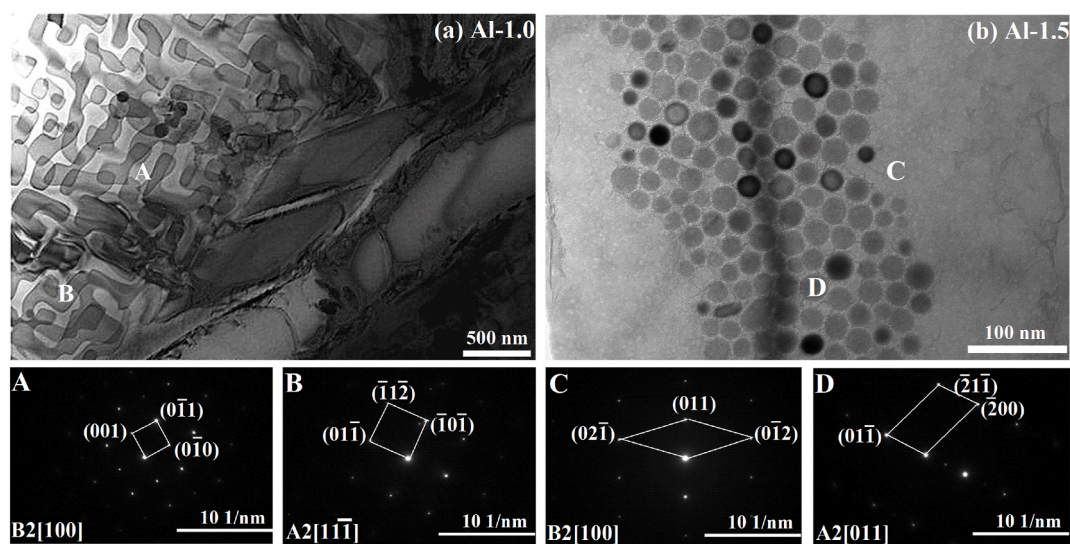


Fig. 4. TEM morphologies and diffraction patterns for the Al-1.0 and Al-1.5 HEAs. The regions marked A, B, C, and D correspond to electron diffraction patterns of the [100], [111], [100], and [011] zone axes.

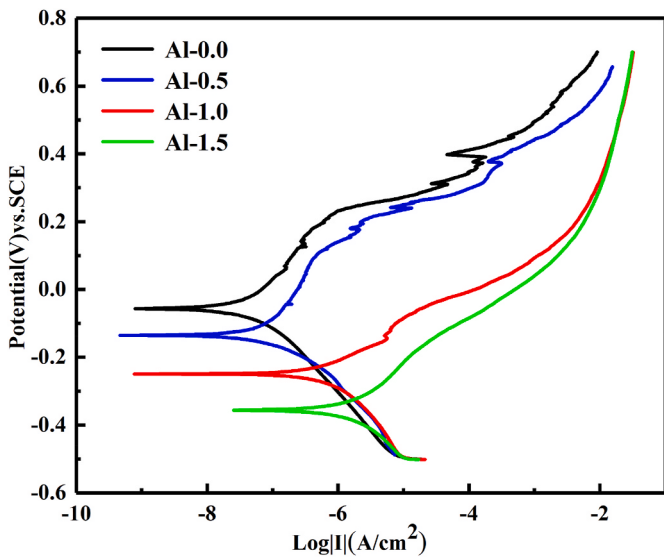


Fig. 5. Representative electrochemical polarization curves of the $\text{Al}_x\text{CoCrFeNi}$ HEAs.

Table 2
Electrochemical data for the $\text{Al}_x\text{CoCrFeNi}$ HEAs.

HEAs	E_{corr} (mV _{SCE})	i_{corr} ($\mu\text{A}/\text{cm}^2$)	E_{pit} (mV _{SCE})	i_{pass} ($\mu\text{A}/\text{cm}^2$)
Al-0.0	-51	3.49×10^{-2}	233	1.06
Al-0.5	-129	6.37×10^{-2}	168	1.89
Al-1.0	-249	4.72×10^{-1}	-98.06	15.95
Al-1.5	-357	1.36×10^0	-145	28.38

investigated and localized corrosion resistance was not considered. Shi et al. [16] prepared $\text{Al}_x\text{CoCrFeNi}$ ($x = 0.3, 0.5$, and 0.7) HEAs with FCC and FCC + BCC phases via a forging process and studied their localized corrosion resistance. The crystal structures of the forged alloys were different from those of the original as-cast alloys, with differences in localized corrosion resistance observed. Furthermore, the localized corrosion resistance of an $\text{Al}_x\text{CoCrFeNi}$ HEA with a single BCC phase has not yet been studied and its corrosion mechanism is not yet known.

The passive film and crystal structure endow an alloy with corrosion resistance and localized corrosion resistance, which are collectively referred to as the “alloy corrosion mechanism” [17,18]. Herein, we prepared $\text{Al}_x\text{CoCrFeNi}$ ($x = 0.0, 0.5, 1.0$, and 1.5 ; molar ratio) HEAs with different crystal structures (FCC, FCC + BCC, and BCC phases). The corrosion mechanisms associated with these $\text{Al}_x\text{CoCrFeNi}$ HEAs were analyzed systematically based on the crystal structures and passivation film in a 3.5 wt% NaCl solution, which provided novel insight for predicting the corrosion mechanisms of $\text{Al}_x\text{CoCrFeNi}$ HEAs with different crystal structures and is consequently useful for corrosion control and future alloy design.

2. Materials and experiments

2.1. Material and sample preparation

$\text{Al}_x\text{CoCrFeNi}$ ($x = 0.0, 0.5, 1.0$, and 1.5 ; molar ratio) HEAs were prepared in vacuum-melting furnaces. The purities of Al, Co, Cr, Fe, and Ni were higher than 99.99%. Ingots weighing ~ 70 g were re-melted at least five times in a water-cooled copper crucible in a high-purity Ar atmosphere to ensure chemical uniformity (the furnace environment achieved a vacuum of 5×10^{-3} Pa). The nominal alloy compositions along with those of the as-cast alloys determined by EDS (in at.%) are listed in Table 1, where the number indicates the molar Al content.

2.2. Corrosion testing

A $10 \times 10 \times 10$ mm test sample was cut via wire cutting. The sample surface was ground using 2000 grit sandpaper. Potential polarization, impedance, and Mott-Schottky experiments were performed using an electrochemical workstation system (DH7000, Jiangsu Donghua Analytical Instruments Co., Ltd.) in 3.5 wt% NaCl solution. Platinum plate was used as the auxiliary electrode, a saturated calomel electrode (SCE) was used as the reference electrode, and the sample was used as the working electrode in a three-electrode system. All electrochemical measurements were conducted at room temperature (25 °C). Working-electrode cathodic polarization was conducted at -800 mV_{SCE} for 5 min to reduce possible surface oxides. Steady-state polarization measurements were conducted at scan rates of 0.2 mV/s; the initial potential was taken as -0.5 V_{SCE}. The sinusoidal impedance potential amplitude was 10 mV, from 100 kHz to 10 mHz. The equivalent circuit corresponding to the impedance data was fitted using ZsimpWin software (Version 3.0). Mott-Schottky measurements were scanned from -1000 to 1000 mV_{SCE} at 10 mV/step and a frequency of 1 kHz. All electrochemical measurements were performed at least three times.

2.3. Chemical and microstructural characterization

The phase compositions of the samples were analyzed via X-ray diffraction (XRD, Shimadzu 7000, Kyoto, Japan) in the $20\text{--}90^\circ$ range at a scan rate of $2^\circ/\text{min}$. The microstructures and surface elements of the samples were observed via scanning electron microscopy (SEM; Gemini 300) and energy dispersion spectroscopy (EDS), respectively. The microstructures of the samples were characterized using electron back-scatter diffraction (EBSD). The passivation film on each sample surface was analyzed using X-ray photoelectron spectroscopy (XPS; ESCALAB250). The sample was examined via transmission electron microscopy (TEM) using a JEM-2100 instrument at 200 kV.

3. Results

3.1. Microstructural characterization

The crystal structures of the $\text{Al}_x\text{CoCrFeNi}$ HEAs were analyzed via XRD (Fig. 1). The Al-0.0 crystal exhibited an FCC structure with (111), (200), and (220) diffraction peaks. The (110) and (211) diffraction peaks observed for Al-0.5 are ascribable to the BCC structure. A diffraction peak for the FCC phase was not observed for Al-1.0, while more intense peaks corresponding to the BCC phase (including the disordered A2 or ordered B2 phase) were observed. A (100) diffraction peak at 32° was observed for Al-1.5, which also corresponds to the BCC phase. The identified $\text{Al}_x\text{CoCrFeNi}$ HEA structures are consistent with expectations and previous results [19].

The microstructures of the $\text{Al}_x\text{CoCrFeNi}$ HEAs are shown in Fig. 2. XRD revealed that Al-0.0 formed a single FCC-phase solid solution (Fig. 2 (a)), while Al-0.5 exhibited coexisting FCC and BCC structures that correspond to dendritic (DR) and inter-dendritic regions (ID) (Fig. 2 (b)). The dendritic regions have the same microstructure as Al-0.0; hence, the dendritic region is composed of the FCC-phase solid solution. The basket-weave-like structures exhibited by the ID regions of Al-0.5 are known to be spinodal-decomposition structures [20,21] with ordered body cubic (B2) and disordered body cubic (A2) crystal structures (inset, Fig. 2 (b)). Grain boundaries and petal-like dendritic structures were observed for Al-1.0 (Fig. 2 (c)). Spinodal-decomposition structures were observed around the grain boundaries of Al-1.0 (inset, Fig. 2 (c)). Hence, XRD revealed that Al-1.0 formed a single BCC phase in solid solution that can be divided into two regions: DR and spinodal decomposition; Yu et al. [22,23] reported similar results. Although DR and ID regions are present in Al-1.5, a basket-weave-like structure was not observed (inset, Fig. 2(d)), which indicates that the spinodal-decomposition mechanism does not persist with increasing Al

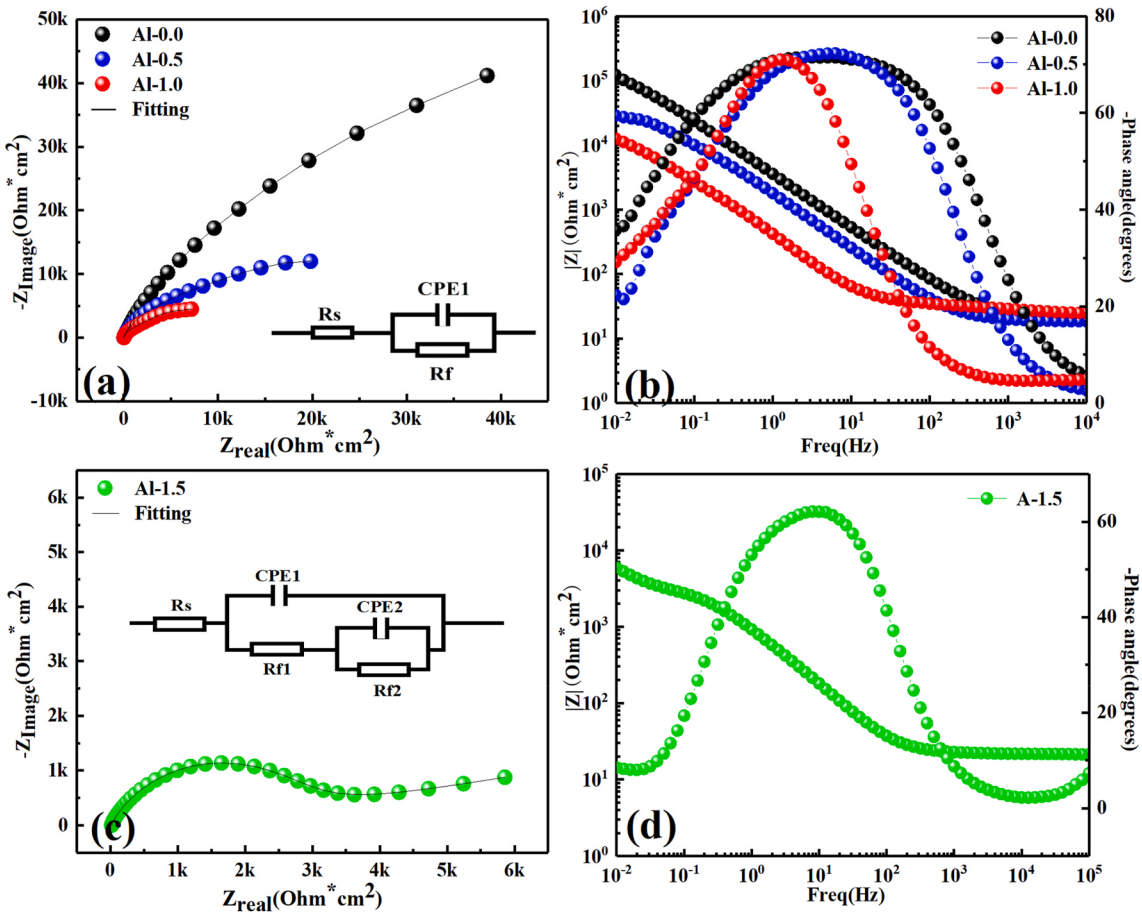


Fig. 6. AC impedance curves for the $\text{Al}_x\text{CoCrFeNi}$ HEAs. (a) (c) Nyquist plots and equivalent circuits. (b) (d) Bode plots.

Table 3
Fitted EIS data.

HEAs	R_s ($\Omega \cdot \text{cm}^2$)	R_{f1} ($\Omega \cdot \text{cm}^2$)	R_{f2} ($\Omega \cdot \text{cm}^2$)	CPE_{1-T} ($\Omega^{-1} \cdot \text{cm}^{-2} \cdot \text{s}^n$)	CPE_{2-T} ($\Omega^{-1} \cdot \text{cm}^{-2} \cdot \text{s}^n$)
Al-0.0	19.42	2.3187×10^5	–	4.1278×10^{-5}	–
Al-0.5	19.64	1.4391×10^5	–	5.8322×10^{-5}	–
Al-1.0	21.14	8.957×10^3	–	7.1864×10^{-5}	–
Al-1.5	21.19	4.153×10^3	1.018×10^3	2.137×10^{-4}	2.682×10^{-2}

content. According to Fig. 1, Al-1.5 formed a single BCC-phase solid solution.

The elemental distributions in Al-0.5 and Al-1.5 were determined by SEM-EDS and are shown in Fig. 3. The FCC phases in the DR regions are composed of elemental Al, Co, Cr, Fe and Ni. The B2 and A2 phases of the spinodal-decomposition structures in the ID regions are composed of Al-Ni and Fe-Cr-Co phases. (Fig. 3(a)–(f)); however, the DR regions in Al-1.5 have different elemental distributions (Fig. 3(g)–(i)) to that of Al-0.5. Each DR region in Al-1.5 is rich in the Al-Ni phase, while the ID region is rich in the Fe-Cr phase, and Co is uniformly distributed.

The compositions of the spinodal-decomposition regions in Al-1.0 and Al-1.5 were determined from their TEM morphologies and diffraction patterns (Fig. 4). In agreement with the basket-weave-like structure observed by SEM, Al-1.0 was identified as comprising the BCC phase with spinodal-decomposition structures (B2+A2) in regions A and B in Fig. 4(a), which was also observed for the $\text{Al}_{0.7}\text{CoCrFeNi}$ and AlCoCrFeNi HEAs [24,25]. Al-1.5 exhibited some nanoscale circular

precipitates with an average radius of ~5 nm that were uniformly distributed on the alloy surface (Fig. 4(b)). The SAED patterns corresponding to C and D identified B2 and A2 phases, respectively. Although Al-1.0 and Al-1.5 exhibited identical electron diffraction spots, their crystal structures were different. Consequently, they exhibit different corrosion morphologies during localized corrosion.

3.2. Corrosion results

3.2.1. Electrochemical polarization testing

The corrosion behavior of the $\text{Al}_x\text{CoCrFeNi}$ HEAs was studied in 3.5 wt% NaCl solution using the Tafel test (Fig. 5). Specific parameters, including the corrosion potential (E_{corr}), corrosion current density (i_{corr}), passivation potential (E_{pit}), and passivation current density (i_{pass}), are listed in Table 2. The value of i_{corr} was obtained using Tafel's linear extrapolation method, where E_{corr} is the ordinate corresponding to i_{corr} . E_{pit} is the potential for which the anodic current increases strongly and i_{pass} is the current density when potential increases and current density changes little. E_{corr} decreased whereas i_{corr} increased with increasing Al content. In general, E_{corr} is closely related to corrosion kinetics, with a higher E_{corr} value corresponding to a lower corrosion tendency. However, E_{corr} cannot be used as the criterion that determines the corrosion resistance of a material, which is primarily determined using the i_{corr} value: a lower i_{corr} corresponds to superior corrosion resistance. The i_{corr} and i_{pass} values were observed to increase in the following order: Al-0.0 > Al-0.5 > Al-1.0 > Al-1.5.

3.2.2. Electrochemical impedance spectroscopy (EIS)

Fig. 6 shows Nyquist and Bode plots for the $\text{Al}_x\text{CoCrFeNi}$ ($x \leq 1.0$) and Al-1.5 HEAs. HEAs with $x \leq 1.0$ exhibit semicircular arcs composed

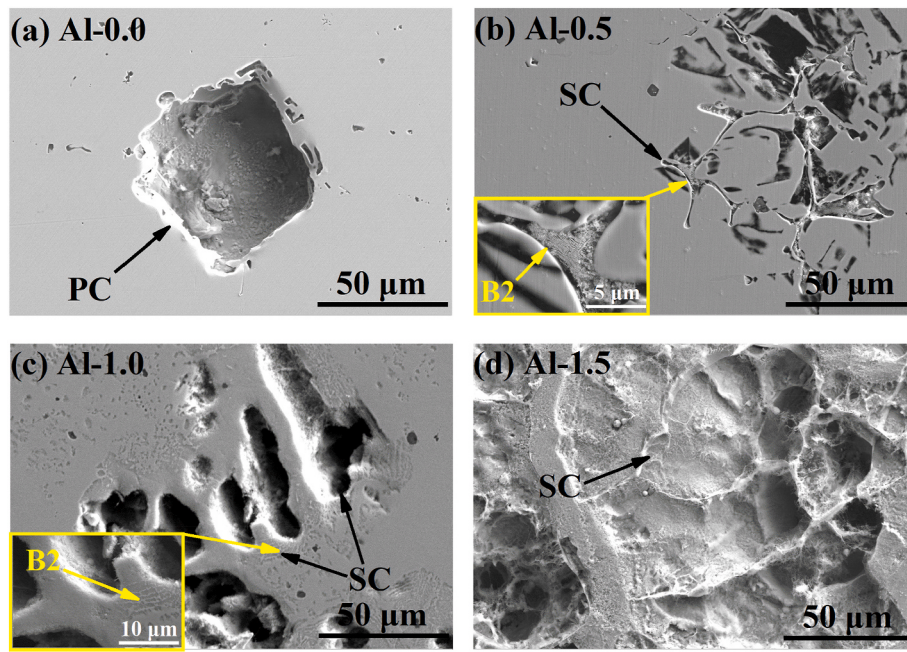


Fig. 7. Corrosion morphologies of the $\text{Al}_x\text{CoCrFeNi}$ HEAs observed by SEM after electrochemical polarization testing.

of high-frequency capacitive arcs, with circle centers below the X-axis, which is normally considered to be associated with charge transfer on non-uniform interfaces (Fig. 6(a)). However, a semicircular arc in the high-frequency region and a line inclined 10° to the X-axis in the low-frequency region were observed for Al-1.5 HEAs. As a result, an equivalent circuit consisting of two parallel parts was established to fit the best experimental result as shown in Fig. 6(c). The corresponding Bode plots (Fig. 6(b) and (d)) show that $|Z|$ decreases with increasing Al content. The electrolyte resistance (R_s), polarization resistance (R_f), and double-layer capacitance of the constant-phase element (CPE_{1-T}), which are listed in Table 3, were used as fitting parameters. R_s was determined to be significantly lower than R_f , which is reasonable. R_f strongly depends on the passivation film and can be considered to be an indicator of the quality of the passive film. R_f decreased from 2.3187×10^5 to $2.759 \times 10^3 \Omega \text{ cm}^2$, which indicates that the protective function of the passive film deteriorates with increasing Al content.

3.3. Morphologies following corrosion testing

The corrosion morphologies of the $\text{Al}_x\text{CoCrFeNi}$ alloys following electrochemical polarization testing are examined using SEM (Fig. 7). Pit-growth positions correspond to positions of weakness in the passive film. The phases that facilitate pit growth can be determined by observing the positions of corrosion pits [26]. Pitting corrosion was randomly distributed in FCC-structured Al-0.0 (Fig. 7(a)), while two-phase Al-0.5 exhibited selective corrosion (SC) in the B2 matrix phase (Fig. 7(b)). Al-1.0 exhibited SC (Fig. 7(c)) in the DR and spinodal-decomposition regions, while it occurred in the DR regions of Al-1.5 (Fig. 7(d))). Corrosion was not observed in the A2 and B2 regions, which is ascribable to the smallness of the A2 and B2 phases. We also found that the four alloys exhibited no dissolved (corroded) grain boundaries.

4. Discussion

The results show that the passivating ability of an $\text{Al}_x\text{CoCrFeNi}$ alloy decreases with increasing Al content. The corrosion mechanisms—including corrosion (composition of the passivation film) and localized corrosion (corrosion type, region, elements etc.)—in

traditional alloys have generally been studied [27,28]. Hence, the corrosion mechanism is discussed here with respect to the passivation film and crystal structure.

4.1. Effect of the passivation film on corrosion

4.1.1. Rapid passivation-film formation

As shown in Fig. 5, passivation regions are evidently present in the $\text{Al}_x\text{CoCrFeNi}$ HEAs. The absence of active–passive transition behavior indicates that the passive film was spontaneously formed during electrochemical polarization testing. Al-0.0 exhibited the widest passivation region; hence, a stable passive film that helps prevent chloride ingress was formed. Al-1.5 exhibited a low corrosion resistance. A single semicircular arc was observed in the Nyquist plot (Fig. 6(a)) whose diameter decreased with increasing Al content. In general, a semicircular arc with a larger diameter corresponds to a more-protective passive film. Thus, Al-0.0 exhibited the best passivation. The corrosion resistance of the protective film on an $\text{Al}_x\text{CoCrFeNi}$ HEA was observed to decrease with increasing Al content.

4.1.2. Composition of the passivation film

The composition of each passivation film was analyzed using XPS (Fig. 8). Co and Ni mostly exist in their metallic states in passivation films, while Fe plays a negligible role in the passivation film of an $\text{Al}_x\text{CoCrFeNi}$ HEA [16]. Therefore, we analyzed the Al and Cr states. XPS revealed that Al and Cr comprise both metallic (Al and Cr) and oxidized/hydrogenated (Al^{3+} and Cr^{3+} ox/hy) valence states.

The Al^{3+}/Al peak-area ratio increased with increasing Al content while the Cr^{3+}/Cr ratio changed little. The Cr peak increasingly fluctuated with increasing Al content, while the Al peak fluctuated less, which indicates that the Cr and Al passivation films become less and more stable, respectively. The oxide/hydroxide groups of Cr^{3+} effectively block Cl^- invasion [29–31], while the oxides/hydroxides of Al^{3+} readily forms porous membrane structures that increase the thickness of the passive film but decrease its density [32,33]. Hence, the addition of Al negatively affects the passivation film.

4.1.3. Type of semiconductor

The Mott–Schottky plots of the $\text{Al}_x\text{CoCrFeNi}$ HEAs were analyzed

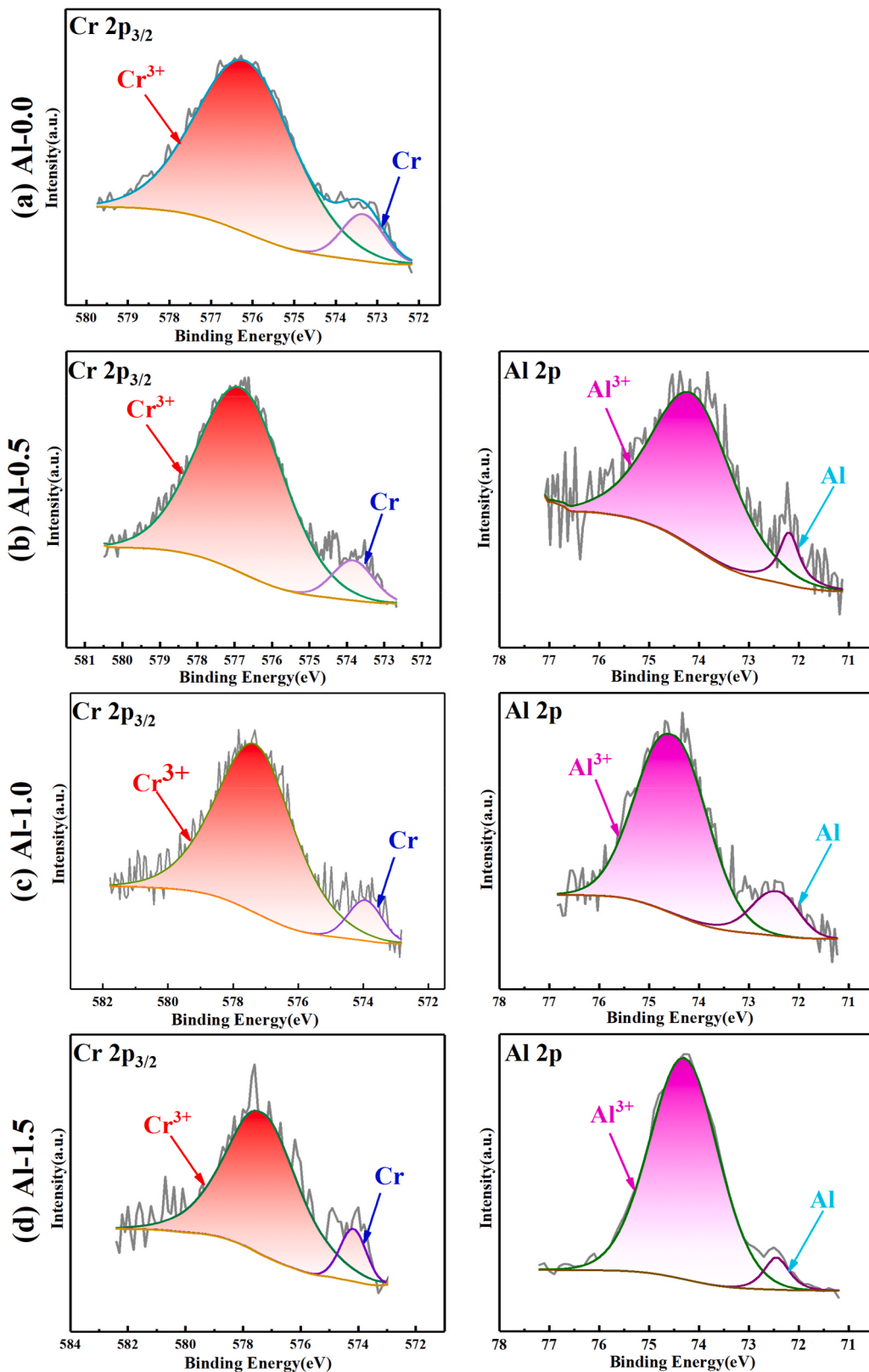


Fig. 8. XPS-determined compositions of Al_xCoCrFeNi HEA passivation films.

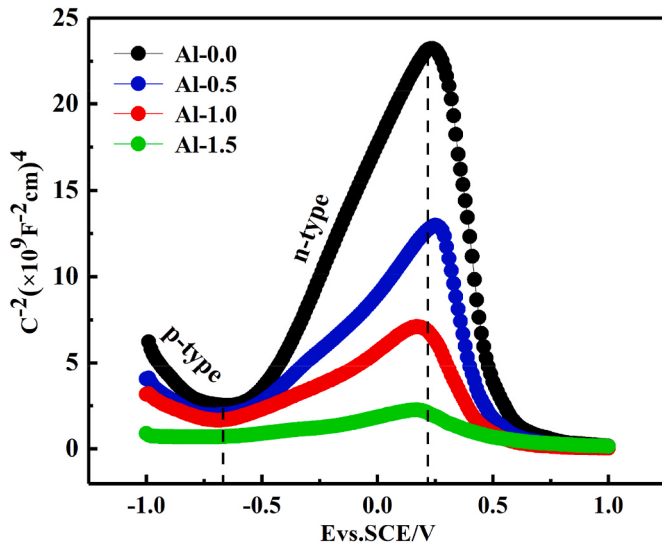


Fig. 9. Mott-Schottky plots for the $\text{Al}_x\text{CoCrFeNi}$ HEAs.

following passivation as shown in Fig. 9, which reveals that each plot has two linear regions, one with a negative slope and the other with a positive slope that correspond to P-type and N-type, semiconductors respectively; hence, the plots display bipolar semiconductor (P–N) characteristics. The intensity of the C^{-2} peaks increases with increasing Al content, with the Al-0.0 HEA exhibiting the highest value; consequently, it shows the lowest capacitance (C). These observations are ascribable to a thicker electron-depletion region or fewer charge carriers; hence, the $\text{Al}_x\text{CoCrFeNi}$ HEA semiconductor type does not change with increasing Al content; rather, the thickness or composition of the passive film becomes modified.

4.2. Effect of crystal structure on corrosion

The crystal structures and phase compositions of $\text{Al}_x\text{CoCrFeNi}$ alloys were determined by EBSD (Fig. 10). The red and green regions in the phase diagrams indicate FCC and BCC phase structures, respectively (Fig. 10(b), (d), (f), and (h)). The volume fraction of the BCC phase increased from 0 to 26.79%, 99.97%, and 100% with increasing Al content. Only a portion of the two grains in Al-0.0 are imaged at the highest EBSD magnification (Fig. 10(a)). Therefore, the Al-0.0 grains were determined to be about 400 μm in size via low-magnification microscopy (inset, Fig. 10(a)). Al-0.5 exhibited smaller grains (350 μm), with the BCC phase distributed in ID regions and the FCC phase distributed in DR regions (Fig. 10(d)). The BCC phase is about 100 μm in size and randomly distributed in the Al-0.5 HEA. The solubility of the BCC phase in the FCC matrix decreases with decreasing temperature during solidification [34,35]. Al-1.0 and Al-1.5 comprise BCC-phase microstructures (Fig. 10(f) and (h)) that are randomly distributed in the alloys. Al-0.0 is a single solid-solution phase with an FCC structure that effectively impedes Cl^- penetration. Moreover, Al-0.0 has a higher grain density, which leads to the formation of a stronger protective interface that prevents Cl^- attack [36]. Therefore, Al-0.0 experiences localized pitting corrosion. Micro-cathodic areas are easily formed in the electrolyte solution, which develops a galvanic-type corrosion cell owing to the potential difference between the DR and ID regions in Al-0.5, Al-1.0, and Al-1.5 [37]. Differences in structure may lead to current coupling [38], which accelerates the localized corrosion of the BCC phase such that SC occurs during the localized corrosion of the three alloys. $\text{Al}_x\text{CoCrFeNi}$ HEAs have coarse-grained structures with mean grain hundreds of microns in size (Fig. 10). Tao et al. [39] reported similar observations. The grains became smaller (from 400 to 200 μm) with increasing Al content, as indicated by the black grain boundaries.

Consequently, Al refines the $\text{Al}_x\text{CoCrFeNi}$ HEA grains. And grain boundaries were observed in the ID regions of Al-0.5 and Al-1.5 (Fig. 10(c) and (g)).

Fig. 11 displays EDS maps showing the element distributions in the $\text{Al}_x\text{CoCrFeNi}$ HEAs before and after corrosion testing. Co, Cr, Fe, and Ni were all corroded in the Al-0.0 sample, which is typical of pitting corrosion. Al and Ni were corroded in Al-0.5 and Al-1.0, respectively, consistent with SC in these two alloy systems, while SC was observed in Al-1.5 and Co was also corroded in addition to Al and Ni. The corroded elements transitioned from (Co, Cr, Fe, and Ni) to (Al and Ni) and then (Al, Ni, and Co), consistent with the EDS maps.

4.3. Corrosion mechanism

We propose a corrosion mechanism for the $\text{Al}_x\text{CoCrFeNi}$ HEAs based on the aforementioned results. The black lines in Fig. 12 show grain boundaries. The $\text{Al}_x\text{CoCrFeNi}$ HEA grains become smaller with increasing Al content, with increasing numbers of grain boundaries observed. The dark blue, and light blue regions correspond to the thickness of Cr and Al passivation film. The yellow region corresponds to the FCC phase (Fig. 12(a)–(d)). Red and purple in Fig. 13(e) and (f) correspond to spinodal-decomposition and dendrite (DR + ID) regions of Al-1.0 HEAs, respectively, while pink and green in Fig. 12(g) and (h) correspond to DR and ID regions of Al-1.5 HEAs, respectively.

Al-0.0 exhibits pitting-corrosion behavior with a corresponding corrosion mechanism consistent with the results shown in Fig. 12(a) and (b). Two passive films are formed: $\text{Cr}_2\text{O}_3/\text{Cr}(\text{OH})_3$ and $\text{Al}_2\text{O}_3/\text{Al}(\text{OH})_3$ (Fig. 12(a)). The $\text{Al}_2\text{O}_3/\text{Al}(\text{OH})_3$ content is low, and $\text{Cr}_2\text{O}_3/\text{Cr}(\text{OH})_3$ plays a dominant role in the passive film, which exhibits good protectability. Passive films are formed in the Cr-poor region, which is a weak area corroded by Cl^- ions. The following anodic dissolution reactions occur in the etched hole: $\text{Co}=\text{Co}^{2+}+2\text{e}^-$, $\text{Cr}=\text{Cr}^{3+}+3\text{e}^-$, $\text{Fe}=\text{Fe}^{3+}+3\text{e}^-$, and $\text{Ni}=\text{Ni}^{2+}+2\text{e}^-$.

Al-0.5 exhibits SC-type corrosion behavior, in which chloride ions attack ID regions composed of the B2 (Al-Ni) phase (Fig. 12(c) and (d)). Owing to the potential difference in the dual-phase FCC + BCC structure, the FCC phase acts as the cathode and the BCC phase acts as the anode for SC; hence, the BCC phase is attacked by chloride ions. The BCC phase is a spinodal-decomposition structure comprising the A2 and B2 phases. The potential difference between A2 and B2 provides a strong driving force for the dissolution of the Cr-poor B2 matrix. The anodic reaction mainly occurring at Al^{3+} and Ni^{2+} .

The presence of many oxides/hydroxides in the Al^{3+} passive film

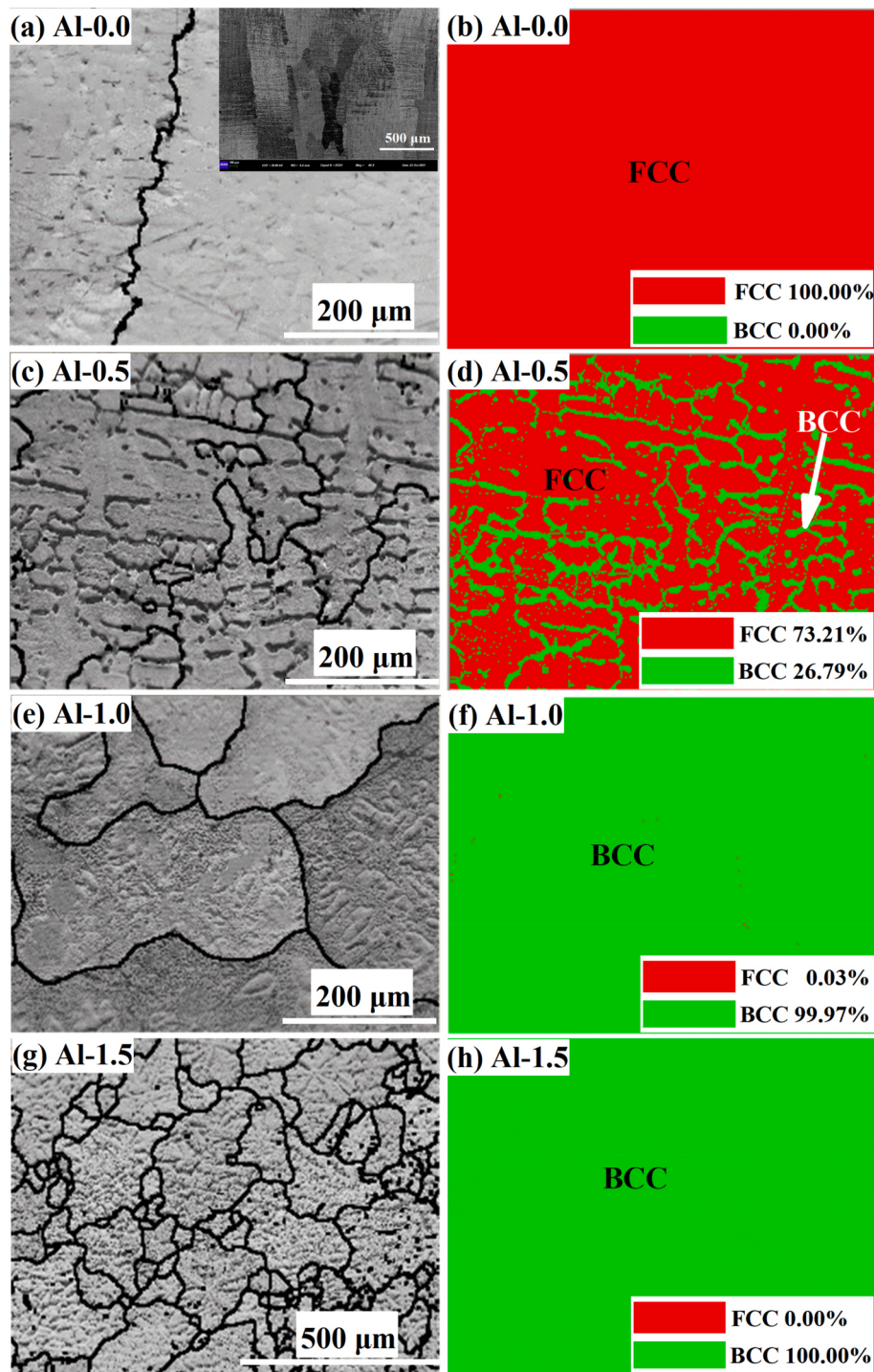


Fig. 10. EBSD images of the $\text{Al}_x\text{CoCrFeNi}$ HEAs. (a), (c), (e), and (g) are band contrast diagrams; (b), (d), (f) and (h) are phase diagrams.

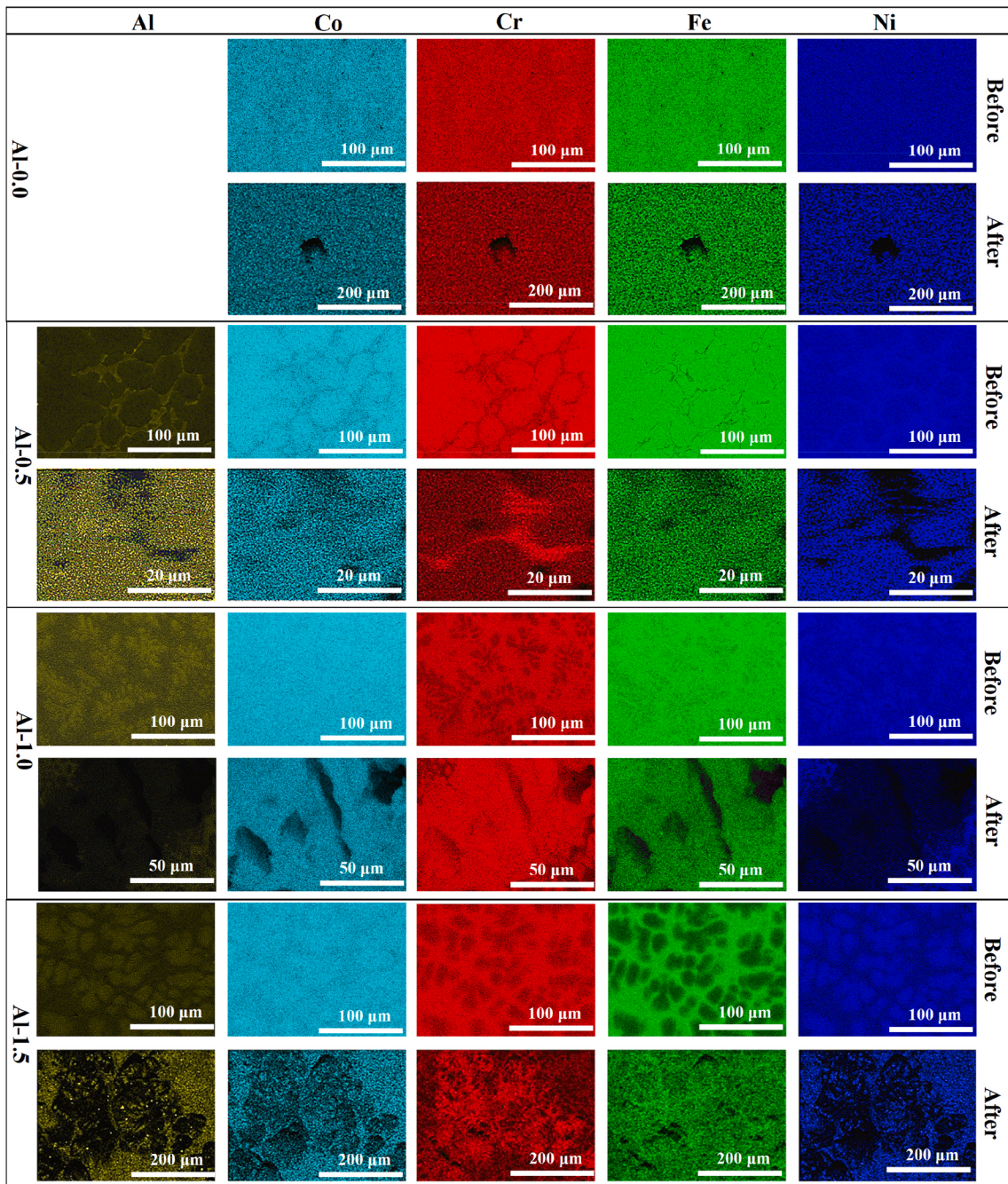


Fig. 11. EDS maps of the surfaces of the $\text{Al}_x\text{CoCrFeNi}$ alloys before and after potentiodynamic polarization experiments.

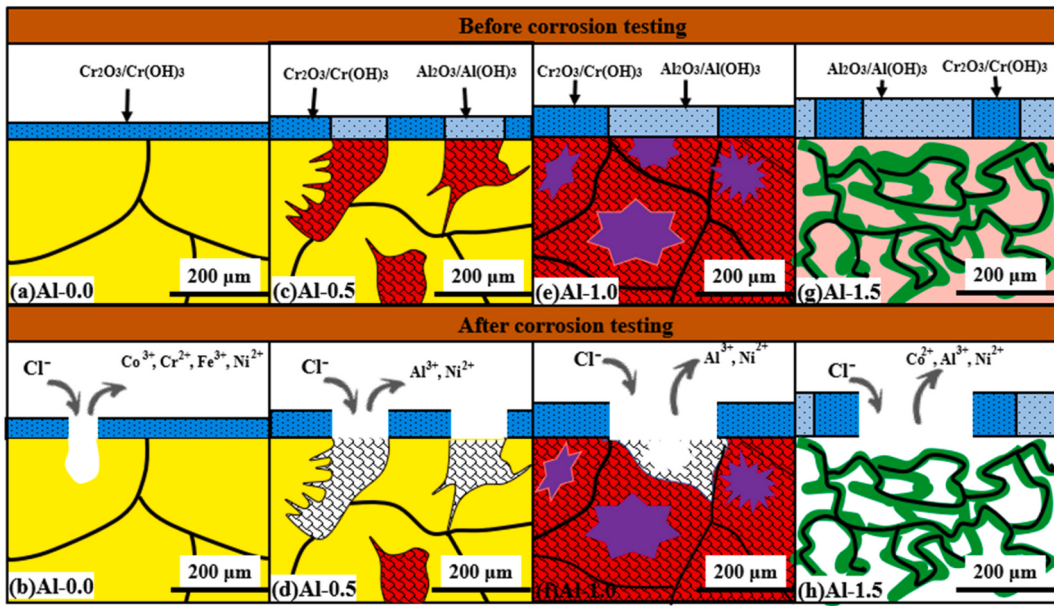


Fig. 12. Schematic depicting the corrosion of $\text{Al}_x\text{CoCrFeNi}$ HEAs.

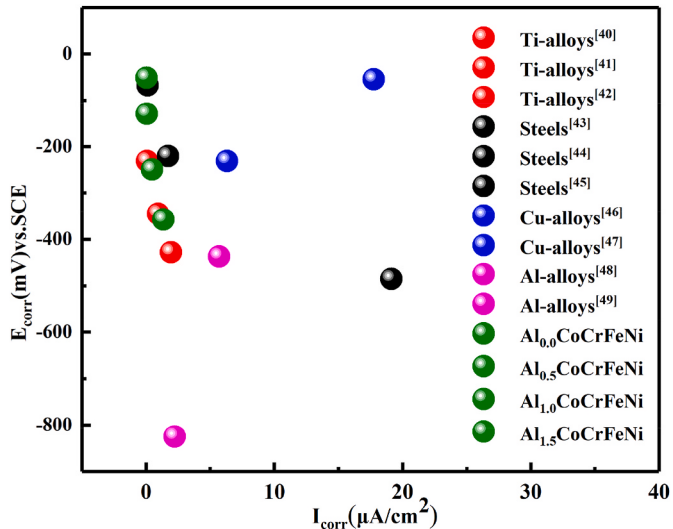


Fig. 13. E_{corr} and i_{corr} for $\text{Al}_x\text{CoCrFeNi}$ HEAs and other traditional alloys.

leads to a less-dense passive film in Al-1.0 (Fig. 12(e)). DR (Al-Ni) regions are preferentially attacked by chloride ions that then corrode the B2 phase (Al-Ni). Al-1.0 contains a single-phase BCC structure with a relatively small potential difference. Nonetheless, Al^{3+} and Ni^{2+} are dissolved due to potential differences.

Al-1.5 has thicker passivation film than the other HEAs. The Al passive film plays a dominant role in a passivation film, leading to a decline in corrosion resistance. Chloride ions increasingly attack the surface of the alloy as the passive film corrodes, with DR (Al-Ni phase) regions and elemental Co becoming corroded, with Al^{3+} , Ni^{2+} , and Co^{2+} dissolved (Fig. 12(h)).

Fig. 13 shows the corrosion potential and current density of $\text{Al}_x\text{CoCrFeNi}$ HEAs and other traditional alloys in 3.5 wt%NaCl solution, including Ti-, Al-, Cu-alloys and steels [40–49]. The E_{corr} and i_{corr} of $\text{Al}_x\text{CoCrFeNi}$ HEAs are much higher than those of Ti-, Al-, Cu-alloys and lie in a comparable band to those of steels, representing the outstanding resistance to corrosion of HEAs in 3.5 wt% NaCl solution. It indicates that $\text{Al}_x\text{CoCrFeNi}$ HEAs may be potential substitutes for structural

materials used in the ocean or other chloride-rich environments.

5. Conclusion

$\text{Al}_x\text{CoCrFeNi}$ HEAs ($x = 0.0, 0.5, 1.0$, and 1.5) were prepared and their corrosion resistances investigated in terms of their passivation films and crystal structures; a corrosion mechanism was also proposed. The following conclusions are drawn:

- 1) The grain size of $\text{Al}_x\text{CoCrFeNi}$ HEAs ($x = 0.0, 0.5, 1.0$, and 1.5) is decreased continuously with increasing Al content, which ranges from 400 to 200 μm .
- 2) Passivation films are formed on $\text{Al}_x\text{CoCrFeNi}$ HEA surfaces, with a competitive relationship between Al and Cr observed. The corrosion resistance of an $\text{Al}_x\text{CoCrFeNi}$ HEA decreases with increasing Al content.

- 3) The $\text{Al}_{0.5}\text{CoCrFeNi}$, $\text{Al}_{1.0}\text{CoCrFeNi}$, and $\text{Al}_{1.5}\text{CoCrFeNi}$ HEAs contain order and disorder body centered cubic structure ($\text{A}2 + \text{B}2$), which affects the localized corrosion behavior of the first two alloys.
- 4) Corrosion type of $\text{Al}_{0.0}\text{CoCrFeNi}$ HEAs is pitting-corrosion behavior, while the obvious selective-corrosion behavior happened on the surface of $\text{Al}_x\text{CoCrFeNi}$ ($x = 0.5, 1.0$ and 1.5) HEAs, the corrosion regions are $\text{B}2$, $\text{DR} + \text{B}2$, and DR regions, respectively.
- 5) This study revealed that $\text{Al}_x\text{CoCrFeNi}$ HEAs exhibit good corrosion resistance and are possible substitutes for structural materials used in the ocean or other chloride-rich environments.

Declaration of competing interest

The authors declare that they have no known competing financial interests or personal relationships that could have appeared to influence the work reported in this paper.

Acknowledgements

This work was supported by the Open Project of the State Key Laboratory of Light Alloy Casting Technology for High-end Equipment, China (LACT-009); the Program for Nature Science Foundation of Liaoning Province, China (2021-BS-150 and 2022-BS-181).

References

- [1] Yeh J-W, Chen S-K, Lin S-J, Gan J-Y, Chin T-S, Shun T-T. Nanostructured high-entropy alloys with multiple principal elements: novel alloy design concepts and outcomes. *Adv Eng Mater* 2004;6:299–303. <https://doi.org/10.1002/adem.200300567>.
- [2] Wang YP, Li BS, Ren MX, Yang C, Fu HZ. Microstructure and compressive properties of AlCrFeCoNi high entropy alloy. *Mater Sci Eng, A* 2008;491:154–8. <https://doi.org/10.1016/j.msea.2008.01.064>.
- [3] Rogachev AS, Kovalev DYU, Kochetov NA, Shchukin AS, Vadchenko SG. Evolution of crystal structure in high-entropy AlCoCrFeNi alloy: an in situ high-temperature X-ray diffraction study. *J Alloys Compd* 2021;861:158562. <https://doi.org/10.1016/j.jallcom.2020.158562>.
- [4] Tang Z, Gao MC, Diao H, Yang T, Liu J, Zuo T, et al. Aluminum alloying effects on lattice types, microstructures, and mechanical behavior of high-entropy alloys systems. *J Occup Med* 2013;65:1848–58. <https://doi.org/10.1007/s11837-013-0776-z>.
- [5] Wang R, Zhang K, Davies C, Wu X. Evolution of microstructure, mechanical and corrosion properties of AlCoCrFeNi high-entropy alloy prepared by direct laser fabrication. *J Alloys Compd* 2017;694:971–81. <https://doi.org/10.1016/j.jallcom.2016.10.138>.
- [6] Lu J, Li L, Chen Y, Liu X, Zhao X, Guo F, et al. Y-Hf co-doped AlCoCrFeNi high-entropy alloy coating with superior oxidation and spallation resistance at 1100°C . *Corrosion Sci* 2021;182:109267. <https://doi.org/10.1016/j.corsci.2021.109267>.
- [7] Strumza E, Hayun S. Comprehensive study of phase transitions in equiatomic AlCoCrFeNi high-entropy alloy. *J Alloys Compd* 2021;856:158220. <https://doi.org/10.1016/j.jallcom.2020.158220>.
- [8] Garip Y, Ergin N, Ozdemir O. Resistance sintering of CoCrFeNiAl_x ($x = 0.7, 0.85, 1$) high entropy alloys: microstructural characterization, oxidation and corrosion properties. *J Alloys Compd* 2021;877:160180. <https://doi.org/10.1016/j.jallcom.2021.160180>.
- [9] Butler TM, Weaver ML. Oxidation behavior of arc melted AlCoCrFeNi multi-component high-entropy alloys. *J Alloys Compd* 2016;674:229–44. <https://doi.org/10.1016/j.jallcom.2016.02.257>.
- [10] Shi Y, Yang B, Xie X, Brechtl J, Dahmen KA, Liaw PK. Corrosion of $\text{Al}_x\text{CoCrFeNi}$ high-entropy alloys: Al-content and potential scan-rate dependent pitting behavior. *Corrosion Sci* 2017;119:33–45. <https://doi.org/10.1016/j.corsci.2017.02.019>.
- [11] Qiu Y, Thomas S, Fabijanic D, Barlow AJ, Fraser HL, Birbilis N. Microstructural evolution, electrochemical and corrosion properties of $\text{Al}_x\text{CoCrFeNi}_{1-x}$ high entropy alloys. *Mater Des* 2019;170:107698. <https://doi.org/10.1016/j.matdes.2019.107698>.
- [12] Kao Y-F, Lee T-D, Chen S-K, Chang Y-S. Electrochemical passive properties of $\text{Al}_x\text{CoCrFeNi}$ ($x = 0, 0.25, 0.50, 1.00$) alloys in sulfuric acids. *Corrosion Sci* 2010;52: 1026–34. <https://doi.org/10.1016/j.corsci.2009.11.028>.
- [13] Huang X, Zhao Q, Zhan Z, Liu J, Liao X, Deng J, et al. Effect of Al addition on the corrosion behavior of $\text{Al}_x\text{CoCrFeNi}$ high entropy alloys in supercritical water. *Corrosion Sci* 2023;216:111089. <https://doi.org/10.1016/j.corsci.2023.111089>.
- [14] Örnek C, Payam B, Gloskovskii A, Kazmanli K, Mohamed N, Derin B, et al. Understanding the passive behaviour of low-chromium high-strength Hybrid steel in corrosive environments. *npj Mater Degrad* 2023;7:71. <https://doi.org/10.1038/s41529-023-00392-z>.
- [15] Izadi M, Soltanieh M, Alalomhoda S, Aghamiri SMS, Mehdizade M. Microstructural characterization and corrosion behavior of $\text{Al}_x\text{CoCrFeNi}$ high entropy alloys. *Mater Chem Phys* 2021;273:124937. <https://doi.org/10.1016/j.matchemphys.2021.124937>.
- [16] Shi Y, Mo J, Zhang F-Y, Yang B, Liaw PK, Zhao Y. In-situ visualization of corrosion behavior of $\text{Al}_x\text{CoCrFeNi}$ high-entropy alloys during electrochemical polarization. *J Alloys Compd* 2020;844:156014. <https://doi.org/10.1016/j.jallcom.2020.156014>.
- [17] Tang Y, Zuo Y, Wang J, Zhao X, Niu B, Lin B. The metastable pitting potential and its relation to the pitting potential for four materials in chloride solutions. *Corrosion Sci* 2014;80:111–9. <https://doi.org/10.1016/j.corsci.2013.11.015>.
- [18] Muangtong P, Rodchanarowan A, Chaysuwan D, Chanlek N, Goodall R. The corrosion behaviour of $\text{CoCrFeNi}-x$ ($x = \text{Cu}, \text{Al}, \text{Sn}$) high entropy alloy systems in chloride solution. *Corrosion Sci* 2020;172:108740. <https://doi.org/10.1016/j.corsci.2020.108740>.
- [19] Klimova M, Shaysultanov D, Semenyuk A, Zherebtsov S, Salishchev G, Stepanov N. B2 precipitates formation in Al-containing CoCrFeMnNi -type high entropy alloy. *IOP Conf Ser Mater Sci Eng* 2021;1014:012018. <https://doi.org/10.1088/1757-899X/1014/1/012018>.
- [20] He JY, Liu WH, Wang H, Wu Y, Liu XJ, Nieh TG, et al. Effects of Al addition on structural evolution and tensile properties of the FeCoNiCrMn high-entropy alloy system. *Acta Mater* 2014;62:105–13. <https://doi.org/10.1016/j.actamat.2013.09.037>.
- [21] Lu J, Chen Y, Zhang H, Ni N, Li L, He L, et al. Y/Hf-doped AlCoCrFeNi high-entropy alloy with ultra oxidation and spallation resistance. *Corrosion Sci* 2020;166: 108426. <https://doi.org/10.1016/j.corsci.2019.108426>.
- [22] Yu W, Qu Y, Li C, Li Z, Zhang Y, Guo Y, et al. Phase selection and mechanical properties of $(\text{Al}_{21.7}\text{Cr}_{15.8}\text{Fe}_{28.6}\text{Ni}_{33.9})_x(\text{Al}_{9.4}\text{Cr}_{19.7}\text{Fe}_{41.4}\text{Ni}_{29.5})_{100-x}$ high entropy alloys. *Mater Sci Eng, A* 2019;751:154–9. <https://doi.org/10.1016/j.msea.2019.02.067>.
- [23] Lu J, Chen Y, Zhang H, Li L, Fu L, Zhao X, et al. Effect of Al content on the oxidation behavior of Y/Hf-doped AlCoCrFeNi high-entropy alloy. *Corrosion Sci* 2020;170: 108691. <https://doi.org/10.1016/j.corsci.2020.108691>.
- [24] Lu J, Chen Y, Zhang H, He L, Mu R, Shen Z, et al. Y/Hf-doped $\text{Al}_{0.7}\text{CoCrFeNi}$ high-entropy alloy with ultra oxidation and spallation resistance at 1200°C . *Corrosion Sci* 2020;174:108803. <https://doi.org/10.1016/j.corsci.2020.108803>.
- [25] Lu J, Li L, Zhang H, Chen Y, Luo L, Zhao X, et al. Oxidation behavior of gas-atomized AlCoCrFeNi high-entropy alloy powder at $900 - 1100^\circ\text{C}$. *Corrosion Sci* 2021;181:109257. <https://doi.org/10.1016/j.corsci.2021.109257>.
- [26] Fu X, Ji Y, Cheng X, Dong C, Fan Y, Li X. Effect of grain size and its uniformity on corrosion resistance of rolled 316L stainless steel by EBSD and TEM. *Mater Today Commun* 2020;25:101429. <https://doi.org/10.1016/j.mtcomm.2020.101429>.
- [27] Wei L, Liu Y, Li Q, Cheng YF. Effect of roughness on general corrosion and pitting of $(\text{FeCoCrNi})_{0.89}(\text{WC})_{0.11}$ high-entropy alloy composite in 3.5 wt.% NaCl solution. *Corrosion Sci* 2019;146:44–57. <https://doi.org/10.1016/j.corsci.2018.10.025>.
- [28] Xuehong X, Deng Y, Shuiqing C, Xiaobin G. Effect of interrupted ageing treatment on the mechanical properties and intergranular corrosion behavior of Al-Mg-Si alloys. *J Mater Res Technol* 2020;9:230–41. <https://doi.org/10.1016/j.jmrt.2019.10.050>.
- [29] Quiambao KF, McDonnell SJ, Schreiber DK, Gerard AY, Freedy KM, Lu P, et al. Passivation of a corrosion resistant high entropy alloy in non-oxidizing sulfate solutions. *Acta Mater* 2019;164:362–76. <https://doi.org/10.1016/j.actamat.2018.10.026>.
- [30] Meng G, Li Y, Shao Y, Zhang T, Wang Y, Wang F. Effect of Cl^- on the properties of the passive films formed on 316L stainless steel in acidic solution. *J Mater Sci Technol* 2014;30:253–8. <https://doi.org/10.1016/j.jmst.2013.07.010>.
- [31] Liu J, Zhang T, Meng G, Shao Y, Wang F. Effect of pitting nucleation on critical pitting temperature of 316L stainless steel by nitric acid passivation. *Corrosion Sci* 2015;91:232–44. <https://doi.org/10.1016/j.corsci.2014.11.018>.
- [32] Shi Y, Collins L, Balke N, Liaw PK, Yang B. In-situ electrochemical-AFM study of localized corrosion of $\text{Al}_x\text{CoCrFeNi}$ high-entropy alloys in chloride solution. *Appl Surf Sci* 2018;439:533–44. <https://doi.org/10.1016/j.apsusc.2018.01.047>.
- [33] Shi Y, Yang B, Rack PD, Guo S, Liaw PK, Zhao Y. High-throughput synthesis and corrosion behavior of sputter-deposited nanocrystalline $\text{Al}_x(\text{CoCrFeNi})_{100-x}$ combinatorial high-entropy alloys. *Mater Des* 2020;195:109018. <https://doi.org/10.1016/j.matdes.2020.109018>.
- [34] Nair RB, Arora HS, Mukherjee S, Singh S, Singh H, Grewal HS. Exceptionally high cavitation erosion and corrosion resistance of a high entropy alloy. *Ultrason Sonochem* 2018;41:252–60. <https://doi.org/10.1016/j.ulsonch.2017.09.044>.
- [35] Li L, Li Z, Kwiatkowski Da Silva A, Peng Z, Zhao H, Gault B, et al. Segregation-driven grain boundary spinodal decomposition as a pathway for phase nucleation in a high-entropy alloy. *Acta Mater* 2019;178:1–9. <https://doi.org/10.1016/j.actamat.2019.07.052>.
- [36] Ralston KD, Birbilis N. Effect of grain size on corrosion: a Review. *Corrosion* 2010; 66. <https://doi.org/10.5006/1.3462912>. 075005-075005–13.
- [37] Xiao DH, Zhou PF, Wu WQ, Diao HY, Gao MC, Song M, et al. Microstructure, mechanical and corrosion behaviors of $\text{AlCoCuFeNi-(Cr,Ti)}$ high entropy alloys. *Mater Des* 2017;116:438–47. <https://doi.org/10.1016/j.matdes.2016.12.036>.
- [38] Kumar N, Fusco M, Komarasamy M, Mishra RS, Bourham M, Murty KL. Understanding effect of 3.5 wt.% NaCl on the corrosion of $\text{Al}_{0.1}\text{CoCrFeNi}$ high-entropy alloy. *J Nucl Mater* 2017;495:154–63. <https://doi.org/10.1016/j.jnucmat.2017.08.015>.
- [39] Shun T-T, Du Y-C. Microstructure and tensile behaviors of FCC $\text{Al}_{0.3}\text{CoCrFeNi}$ high entropy alloy. *J Alloys Compd* 2009;479:157–60. <https://doi.org/10.1016/j.jallcom.2008.12.088>.
- [40] Delgado-Alvarado C, Sundaram PA. A study of the corrosion behavior of gamma titanium aluminide in 3.5 wt.% NaCl solution and seawater. *Corrosion Sci* 2007;49: 3732–41. <https://doi.org/10.1016/j.corsci.2007.04.001>.

- [41] Su BX, Luo LS, Wang BB, Su YQ, Wang L, Ritchie RO, Guo EY, Li T, Yang HM, Huang HG, Guo JG, Fu HZ. Annealed microstructure dependent corrosion behavior of Ti-6Al-3Nb-2Zr-1Mo alloy. *J Mater Sci Technol* 2021;62:234–48. <https://doi.org/10.1016/j.jmst.2020.05.058>.
- [42] Bodunrin MO, Chown LH, Merwe JW, Alaneme KK. Corrosion behaviour of Ti-Al-xV-yFe experimental alloys in 3.5 wt% NaCl and 3.5 M H₂SO₄. *Mater Corros* 2018; 69:1–11. <https://doi.org/10.1002/maco.201709709>.
- [43] Sarkar PP, Kumar P, Manna MK, Chakraborti PC. Microstructural influence on the electrochemical corrosion behaviour of dual-phase steels in 3.5% NaCl solution. *Mater Lett* 2005;59:2488–91. <https://doi.org/10.1016/j.matlet.2005.03.030>.
- [44] Almomani MA, Hayajneh MT, Al-Daraghmeh MY. Corrosion resistance of TiO₂-ZrO₂ nanocomposite thin films spin coated on AISI 304 stainless steel in 3.5 wt. % NaCl solution. *Mater Res* 2019;22(5):e20190014. <https://doi.org/10.1590/1980-5373-MR-2019-0014>.
- [45] Kumar N, Singh AK, Kumar A, Kumar S, Patel S. Corrosion behaviour of austenitic stainless steel (grade 316) in 3.5 wt % NaCl. *Int J Sci Res* 2014;2:1029–36.
- [46] Li WH, Hu LC, Zhang ST, Hou BR. Effects of two fungicides on the corrosion resistance of copper in 3.5% NaCl solution under various conditions. *Corrosion Sci* 2011;53:735–45. <https://doi.org/10.1016/j.corsci.2010.11.006>.
- [47] Zhu JJ, Li SH, Shen LN, Yang WL, Li Z. Corrosion behavior of novel Cu–Ni–Al–Si alloy with super-high strength in 3.5% NaCl solution. *Trans Nonferrous Metals Soc China* 2017;27:1096. [https://doi.org/10.1016/S1003-6326\(17\)60128-6](https://doi.org/10.1016/S1003-6326(17)60128-6), 04.
- [48] Shosh R, Venugopal A, Ramesh Narayanan P, Sharma SC, Venkitakrishnan PV. Environmentally assisted cracking resistance of Al–Cu–Li alloy AA2195 using slow strain rate test in 3.5% NaCl solution. *Trans Nonferrous Metals Soc China* 2017;27:241–9. [https://doi.org/10.1016/S1003-6326\(17\)60028-1](https://doi.org/10.1016/S1003-6326(17)60028-1).
- [49] Hazwan Hussin M. Electrochemical data of single and hybrid sol-gelcoating precursors for aluminum alloy corrosion protection in 3.5% NaCl. *Data Brief* 2019; 22:971–6. <https://doi.org/10.1016/j.dib.2019.01.029>.